Nucleation and growth of feitknechtite from nanocrystalline vernadite precursor

Sylvain Grangeon, Fabienne Warmont, Christophe Tournassat, Bruno Lanson, Martine Lanson, Erik Elkaim, Francis Claret

Eur. J. Mineral.
2017, **29**, 767–776
Published online 26 June 2017

Special issue dedicated to Zdeněk Johan

Nucleation and growth of feitknechtite from nanocrystalline vernadite precursor

Sylvain GRANGEON[1,*], Fabienne WARMONT[2], Christophe TOURNASSAT[1,3], Bruno LANSON[4], Martine LANSON[4], Erik ELKAÏM[5] and Francis CLARET[1]

[1] D3E/SVP, BRGM (French Geological Survey), 3 Avenue Claude Guillemin, 45060 Orléans, France
*Corresponding author, e-mail: s.grangeon@brgm.fr
[2] ICMN – CNRS – Université d'Orléans, 1b rue de la Férollerie, 45071 Orléans Cedex 2, France
[3] UMR 7327 Institut des Sciences de la Terre d'Orléans, Université d'Orléans – CNRS/INSU – BRGM, 45071 Orléans, France
[4] Univ. Grenoble Alpes, CNRS, ISTerre, 38000 Grenoble, France
[5] Synchrotron Soleil, L'Orme des Merisiers Saint-Aubin, BP 48, 91192 Gif-sur-Yvette Cedex, France

Abstract: Vernadite is a nanocrystalline manganese oxide, which controls the fate of many trace elements in soils and sediments through sorption and oxidative-degradation mechanisms. This exceptional reactivity directly results from its crystal structure, which may however evolve upon contact with redox-sensitive species. Understanding these changes is a prerequisite to predict and model the geochemical cycle of trace elements in the environment. Here, the structural and morphological modifications affecting synthetic nanocrystalline vernadite (δ-MnO_2) upon contact with increasing concentrations of Mn^{2+} were investigated using wet chemistry, synchrotron X-ray diffraction and transmission electron microscopy. Fresh δ-MnO_2 crystals had an Mn oxidation state of 3.94 ± 0.05 and a ~10 Å layer-to-layer distance. Crystal size was ~10 nm in the layer plane, and ~1 nm perpendicular to that. Upon contact with aqueous Mn^{2+} under anoxic conditions, δ-MnO_2 crystals underwent several morphological and mineral evolutions, starting with the stacking, perpendicular to the layer plane, of δ-MnO_2 crystals to form crystals ~10 nm × 2 nm which were then subjected to oriented aggregation both along and perpendicular to the layer plane to form lath-like crystals with dimensions of ~100 nm × 20 nm. Finally, these laths stacked perpendicular to the layer plane to form synthetic feitknechtite (β-MnOOH) crystals with sizes up to ~100 nm × 500 nm when the Mn^{2+} loading reached 31.9 mmol g^{-1}. Structural transformation from δ-MnO_2 to synthetic feitknechtite was detected at Mn^{2+} loading equal to or higher than 3.27 mmol g^{-1}.
These mechanisms are likely to influence the geochemical fate of trace elements in natural settings where Mn^{2+} is abundant. Firstly, the systematic increase in crystal size with increasing Mn^{2+} loading may impact the sorption capacity of vernadite and feitknechtite by reducing the density of reactive edge sites. Secondly, the fate of trace elements initially sorbed at the vernadite surface is unclear, as they could either be released in solution or incorporated into the feitknechtite lattice.

Key-words: vernadite; δ-MnO_2; feitknechtite; β-MnOOH; manganese oxide; X-ray diffraction; transmission electron microscopy; nucleation; sorption; crystal growth.

1. Introduction

Manganese (Mn) oxides are ubiquitous in surficial environments, where they play a key role in the geochemical cycles of major and trace elements, as they are highly reactive towards nutrients (*e.g.*, Xin *et al.*, 2016), metals (*e.g.*, Halbach, 1986; Bellanca *et al.*, 1996; Manceau *et al.*, 2004, 2007, 2014; Marcus *et al.*, 2004; Boonfueng *et al.*, 2006; Fuller & Bargar, 2014), actinides (*e.g.*, Kunzendorf & Friedrich, 1976; Koppi *et al.*, 1996; Duff *et al.*, 1999) and organic matter and organic molecules (*e.g.*, Cheney *et al.*, 1996; Nasser *et al.*, 2000; Barrett & McBride, 2005; Chang Chien *et al.*, 2009; Johnson *et al.*, 2015). Vernadite, the nanocrystalline and turbostratic analogue to birnessite (Giovanoli, 1980), is one of most abundant (Taylor *et al.*, 1964; Taylor, 1968; Ross *et al.*, 1976; Birnie & Paterson, 1991) and reactive Mn oxides, especially in suboxic aqueous systems such as the upper soil. The vernadite structure consists in the turbostratic stacking of layers of $(Mn^{4+}O_6)^{8-}$ octahedra connected through their edges and separated from each other by hydrated interlayer cations (*e.g.*, Giovanoli, 1980; Chukhrov *et al.*, 1985; Jurgensen *et al.*, 2004; Villalobos *et al.*, 2006; Grangeon *et al.*, 2008). In natural settings, vernadite mainly has hexagonal layer symmetry (*e.g.*, Marcus *et al.*, 2004; Manceau *et al.*, 2007, 2014; Bargar *et al.*, 2009). These layers may contain vacancies and/or isomorphic substitutions of Mn^{4+} by cations of lower

DOI: 10.1127/ejm/2017/0029-2665
0935-1221/17/0029-2665 $ 4.50

valence (*e.g.*, Mn^{3+}, Ni^{2+}, Co^{3+}; Manceau *et al.*, 1997, 2014; Peacock & Sherman, 2007; Lanson *et al.*, 2008; Peña *et al.*, 2010; Grangeon *et al.*, 2014) which, together with the minute size of the layers (5–10 nm, *e.g.*, Hochella *et al.*, 2005; Bargar *et al.*, 2009), are responsible for the exceptional reactivity of vernadite. The possible contact with redox-sensitive species such as Mn^{2+} can induce structural changes whose nature and extent depend on solution pH and Mn^{2+} concentration. The first step of reaction between aqueous Mn^{2+} and layer Mn^{4+}, hereafter referred to as $Mn^{2+}_{(aq)}$ and $Mn^{4+}_{(s)}$, respectively, is (Elzinga, 2016):

$$Mn^{2+}_{(aq)} + Mn^{4+}_{(s)} \rightarrow 2Mn^{3+}_{(s)},$$

where $Mn^{3+}_{(s)}$ is layer Mn^{3+}. The $2Mn^{3+}_{(s)}$ formed may further disproportionate, returning the system to its initial state. Alternatively, they may accumulate in the structure and induce a change in layer symmetry, from hexagonal to orthogonal, as observed experimentally at pH 9 when the molar ratio of Mn^{2+} to δ-MnO_2 is lower than 0.05 (Zhao *et al.*, 2016). At lower pH and/or at higher Mn^{2+} concentration, a transformation to synthetic feitknechtite (β-MnOOH) is observed, following the reaction:

$$\delta\text{-}Mn^{4+}O_2 + Mn^{2+}_{(aq)} \rightarrow 2\beta\text{-}Mn^{3+}OOH.$$

Feitknechtite, whose structure is built of layers of $(Mn^{3+}O_6)^{9-}$ octahedra, may upon ageing convert to manganite (γ-MnOOH) at pH 7.0–7.5 or to hausmannite (Mn_3O_4) at pH > 8 (Elzinga, 2011; Lefkowitz *et al.*, 2013; Lefkowitz & Elzinga, 2015).

The interplay between these structural transformations certainly influences the geochemical cycle of trace elements by modifying the reactivity of Mn oxides through a change in the nature and density of local crystal charges, but also by modifying the fate of trace elements initially adsorbed at the vernadite surface which, by analogy with the phyllomanganate-to-tectomanganate transformation, could either be incorporated in the structure during transformation or released to solution (Atkins *et al.*, 2014, 2016; Grangeon *et al.*, 2015).

The present study aimed at contributing to a better understanding of the vernadite-to-feitknechtite transformation, and in particular at elucidating the reaction mechanisms at the crystal scale, using wet chemistry, X-ray diffraction (XRD) and transmission electron microscopy (TEM).

2. Materials and methods

2.1. Sample synthesis, sorption experiments and chemical analyses

The δ-MnO_2 phase was synthesized using a redox method described elsewhere (Villalobos *et al.*, 2003). The average oxidation state (AOS) of Mn was determined by using a potentiometric method (Grangeon *et al.*, 2012). After synthesis, samples were Na-saturated through ten cycles of centrifugation, supernatant removal and resuspension in a 1 M NaCl solution. A last step of three similar cycles with de-ionized water instead of 1 M NaCl was then performed. The obtained δ-MnO_2 paste was immediately freeze-dried, and the resulting powder was introduced in a N_2-filled glove box where it was left for ~7 d. Eight aliquots of ~20–40 mg powder each were then introduced in previously weighted dialysis membranes. Filled membranes were weighted, filled with a solution containing 0.1 M NaCl and $MnCl_2$ at a concentration ranging 0–0.04 M, sealed, and introduced in 50 mL polypropylene tubes, to which 40.5–45 mL of the solution introduced in the dialysis membrane were added. Initial solution pH was 6.5. Tubes were sealed and left to agitate for 24 h. The dialysis membrane was then separated from the solution whose final pH ranged between 6.5 and 5.8. The solution was acidified to pH ~3 with HNO_3 and analyzed for its Mn^{2+} content using an ICP-AES (Horiba-Jobin Yvon Ultima 2). The magnitude of Mn^{2+} retention by δ-MnO_2 was quantified using the R_D factor (Tournassat *et al.*, 2013) defined as:

$$R_D = \frac{C_{init} - C_{aqu}}{C_{aqu} \times R_{SL}},$$

where C_{init} is the initial concentration of Mn^{2+}, C_{aqu} the Mn^{2+} concentration in solution after equilibration, and R_{SL} is the solid-to-liquid ratio in the experiment (in kg L^{-1}).

The dialysis membrane was opened and the solid separated by filtration (0.01 μm cut-off) before being washed with bi-distilled water. An aliquot was freeze-dried for TEM analysis, whereas the remaining was sealed in a polyimide capillary for XRD analysis in the wet state within 48 h. Samples were labelled MndBi-XX, where XX is the Mn^{2+} loading (in mmol Mn^{2+} per g of dry δ-MnO_2).

2.2. Synchrotron X-ray diffraction

The XRD experiments were carried out at station CRISTAL (SOLEIL synchrotron in Orsay, France), using an energy of 28.44 keV (λ = 0.436 Å) and an XPad hybrid pixel detector. Data were recorded over the 1.2–124.5° 2θ range with a total collection time of 30 min and processed with a specific software (Ounsy *et al.*, 2013). To ease comparison with previous studies (*e.g.*, Grangeon *et al.*, 2015, 2017), diffraction data will be expressed relative to the scattering vector q, where $q = [4 \times \pi \times \sin(\theta)]/\lambda$.

2.3. Transmission electron microscopy

The TEM experiments were carried out using a Philips CM20 microscope operated at 200 kV. Prior to observation, samples were embedded in epoxy resin, left to polymerize for 48 h in the dark and cut with an ultramicrotome (Reichert-Jung Ultra-cut E) equipped with a diamond knife. The ~80 nm thick sections were picked up on lacey carbon films loaded on Cu grids. In addition, to assess possible preparation-induced artefacts (use of an ultramicrotome), a sample identical to MndBi-0.5 (Table 1) was prepared according to the above described protocol, filtered and

Table 1. Experimental conditions of δ-MnO_2 contacts with $Mn^{2+}_{(aq)}$ and chemical characterization of reacted solids.

Sample	Mn AOS	Mn^{2+}_{sorbed} (mmol g^{-1})	C_{aqu} (mmol L^{-1})	R_{SL} (g L^{-1})	log(R_D) (R_D in L kg^{-1})
MndBi-0	3.94 ± 0.05	n.d.	n.d.	0.65	n.d.
MndBi-0.5	3.80 ± 0.05	0.49	0.03	0.70	4.21
MndBi-1.5	n.d.	1.49	0.41	0.68	3.56
MndBi-3.3	3.54 ± 0.10	3.27	0.94	0.73	3.54
MndBi-8.6	n.d.	8.61	2.41	0.49	3.55
MndBi-11.3	n.d.	11.32	6.35	0.91	3.25
MndBi-28.1	3.62[a]	28.05	12.15	0.64	3.36
MndBi-31.9	n.d.	31.90	20.47	0.55	3.19

Notes: Mn^{2+} loading at the end of the experiment (Mn^{2+}_{sorbed}) is the number of mmol of Mn^{2+} sorbed per g of δ-MnO_2. n.d. stands for "not determined".
[a] May be subject to high uncertainties as a single measurement was performed.

re-suspended in alcohol. A drop of the obtained suspension was deposited on a Cu grid. Fast-Fourier transform (FFT) analysis of the micrographs was done with ImageJ (Schneider *et al.*, 2012).

3. Results and discussion

3.1. Determination of Mn^{2+} retention coefficient

An increase in $Mn^{2+}_{(aq)}$ resulted in a decrease in the Mn AOS of the final solids, suggesting retention of Mn^{2+} on δ-MnO_2 (Table 1). The R_D values (Table 1) compared well with previously reported values obtained after 8 d of equilibration (Fig. 1). The evolution of R_D as a function of Mn^{2+} concentration and pH (Murray, 1975) has, in some cases, been interpreted in terms of adsorption and quantified in surface-complexation models (Appelo & Postma, 1999; Tonkin *et al.*, 2004). Data interpreted with these models had a Mn^{2+} loading ranging from 1 to 12 Mn^{2+} per nm^2, depending on the dataset and on the specific surface area considered (value measured by the authors or 600 m^2 g^{-1} as recommended by Tonkin *et al.*, 2004). Such loading roughly corresponds to MndBi-1.5 (1.5 Mn^{2+} per nm^2 assuming a specific surface area of 600 m^2 g^{-1}), which means that this sample and MndBi-0.5 could have been interpreted in the frame of these models. For other samples, the density of Mn^{2+} at the surface of δ-MnO_2 would be unrealistically high (up to 32 Mn^{2+} per nm^2 for MndBi-31.9), and interaction of Mn^{2+} with δ-MnO_2 most likely resulted in a structure transformation, which was studied by XRD.

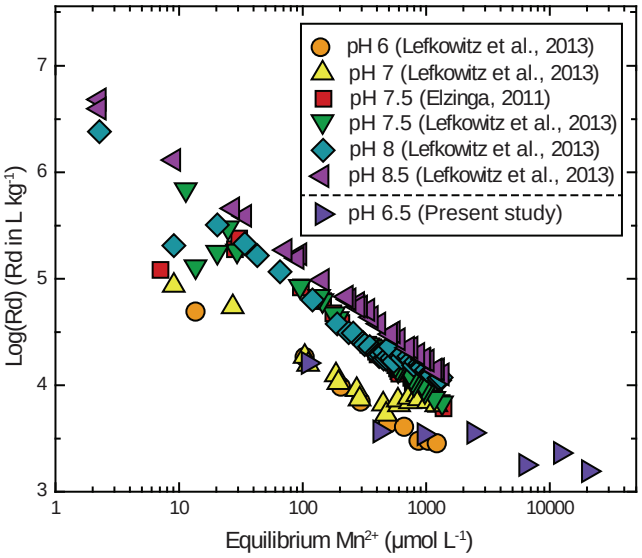

Fig. 1. Evolution of the Mn^{2+} retention coefficient as a function of Mn^{2+} concentration. Patterns are indicative of the experiment pH: circles and triangles pointing up, experiments conducted at pH 6 and pH 7, respectively; squares and triangles pointing down, pH 7.5; diamonds, pH 8; triangles pointing left, pH 8.5 (Elzinga, 2011; Lefkowitz *et al.*, 2013). Published data were collected with a contact time of 8 d. Present data (pH 6.5; 1 d contact time) are shown as triangles pointing right.

3.2. Mineralogical evolution

Two sets of reflections could be observed in the XRD pattern of MndBi-0 (Fig. 2), which was not in contact with Mn^{2+}, both being consistent with a nanocrystalline turbostratic phyllomanganate structure. The first set corresponded to broad and asymmetric reflections at 2.58 $Å^{-1}$, 4.42 $Å^{-1}$ and 5.11 $Å^{-1}$ (*d*-spacing of 2.44 Å, 1.42 Å and 1.23 Å). The reflection at 4.42 $Å^{-1}$ was shown to be indicative of layer symmetry: approximately symmetric when layer symmetry is hexagonal, but split in two distinct maxima when layer symmetry is orthogonal (Drits *et al.*, 2007). Here, it was symmetric despite the presence of a shoulder on the low-*q* side, related to a basal reflection (see below), and layer symmetry was hexagonal. For consistency with previous studies (*e.g.*, Lanson *et al.*, 2000, 2008; Webb *et al.*, 2005; Drits *et al.*, 2007; Grangeon *et al.*, 2010, 2012; Zhu *et al.*, 2010; Manceau *et al.*, 2013), bands were indexed with an orthogonal symmetry system ($a = \sqrt{3} \times b$, $\gamma = 90°$) and the three maxima were indexed as (11, 20), (31, 02) and (22, 40) *hk* band, respectively. Reflections of the second set were sharp and symmetric and formed a rational series of 00*l* reflections at 0.62 $Å^{-1}$, 1.24 $Å^{-1}$ and 1.85 $Å^{-1}$ (10.15 Å, 5.08 Å and 3.39 Å). The layer-to-layer distance, inferred from the position of the 003 at 1.85 $Å^{-1}$, was 10.17 Å. When increasing Mn^{2+} loading up to 1.5 mmol g^{-1} (MndBi-1.5), the intensity of the 00*l* reflections decreased, but the position remained essentially unchanged and

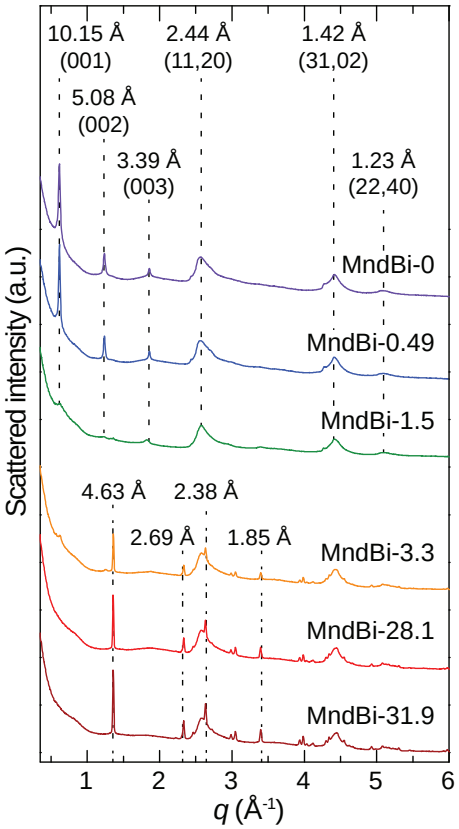

Fig. 2. From top to bottom, XRD patterns of MndBi-0, MndBi-0.5, MndBi-1.5, MndBi-3.3, MndBi 28.1 and MndBi-31.9. Dashed lines and dashed-dotted lines point out to the presence of diffraction maxima of δ-MnO_2 and synthetic feitknechtite, respectively.

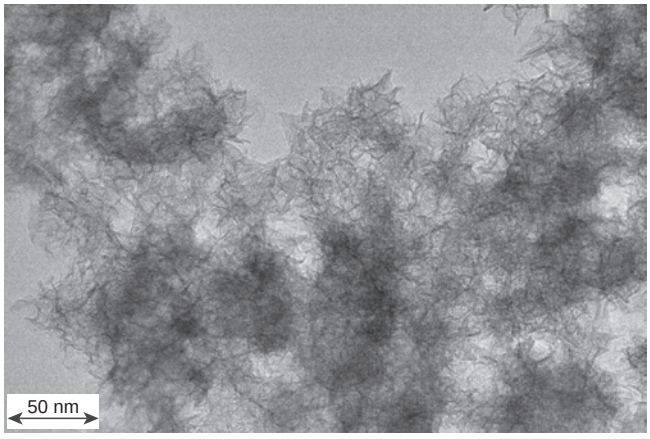

Fig. 3. Transmission electron microscope (TEM) observation of type 1 crystals from MndBi-0.

hk bands were unaffected. The shoulder on the low-*q* side of the (31, 02) band weakened, supporting its indexation as the 006 reflection. Note the presence of a weak peak at ~1.36 $Å^{-1}$ (~4.6 Å) in the XRD pattern of MndBi-1.5, which could be attributed to synthetic feitknechtite (see below). Weakening of 00*l* reflections can be interpreted as a loss of parallelism between adjacent layers and was attributed to the incorporation of $Mn^{3+}_{(s)}$ according to the comproportionation mechanism described above. Indeed, Mn^{3+} octahedra are distorted by the Jahn–Teller effect and their presence within the octahedral layer induces strains that ultimately lead to layer kinking (Webb *et al.*, 2005; Atkins *et al.*, 2014; Grangeon *et al.*, 2014) and subsequent loss of parallelism between layers. In addition to *hk* bands of δ-MnO_2, the XRD pattern of MndBi-3.3 (3.3 Mn^{2+} per nm^2) had additional reflections, *e.g.*, at 1.36 $Å^{-1}$, 2.34 $Å^{-1}$, 2.64 $Å^{-1}$ and 3.40 $Å^{-1}$ (4.63 Å, 2.69 Å, 2.38 Å, and 1.85 Å), assigned to synthetic feitknechtite (Bricker, 1965). As the latter reflections became more intense with increasing Mn^{2+} loading, up to 31.90 mmol g^{-1} (MndBi-31.9), the proportion of synthetic feitknechtite increased with Mn^{2+} loading.

Such an evolution was consistent with previous studies (Elzinga, 2011, 2016; Lefkowitz *et al.*, 2013; Lefkowitz & Elzinga, 2015). In the following section, the mechanisms of transformation were studied at the crystal scale, hypothesizing that an increased concentration of Mn^{2+} led to an increased conversion of δ-MnO_2 to synthetic feitknechtite without significant dissolution of δ-MnO_2. In other words, it was hypothesized that the structural and morphological evolution of samples following their contact with a given concentration of $Mn^{2+}_{(aq)}$ underwent intermediate recrystallization steps similar to those observed during *post-mortem* analysis of samples in contact with lower concentrations of $Mn^{2+}_{(aq)}$. This hypothesis is supported by previous TEM observations, from which it was concluded that there was a lack of significant dissolution/reprecipitation during the recrystallization of δ-MnO_2 when in contact with aqueous $MnSO_4$ (Tu *et al.*, 1994). Absence of δ-MnO_2 dissolution is further substantiated by the study of Elzinga & Kustka (2015) showing that the first steps of transformation involves solely comproportionation and disproportionation reactions induced by interfacial electron transfer between adsorbed Mn^{2+} and $Mn^{4+}_{(s)}$. Experimental validation of this hypothesis would require performing a kinetic experiment at high $Mn^{2+}_{(aq)}$ concentration to check whether recrystallization steps observed as a function of Mn^{2+} concentration are similar to those occurring as a function of time. Such a procedure was applied to the study of the δ-MnO_2 to synthetic todorokite transformation (Atkins *et al.*, 2014, 2016), but was not possible in the present case because of reaction kinetics. The R_D values obtained in the present study after 1 d of contact time were identical to those reported previously for a contact time of 8 d (Fig. 1). Steady-state was thus reached in less than 1 d of contact time, consistent with previous observations showing that feitknechtite is formed in less than 20 min (Johnson *et al.*, 2016) and that sorption of Mn^{2+} at the δ-MnO_2 surface is completed within less than 1 s (Fendorf *et al.*, 1993).

3.3. Morphological evolution during δ-MnO_2 to synthetic feitknechtite transformation

Sample MndBi-0 consisted of crystals ~10 nm in their largest dimension (presumably the layer plane) and ~1 nm perpendicular (Fig. 3), henceforth denominated

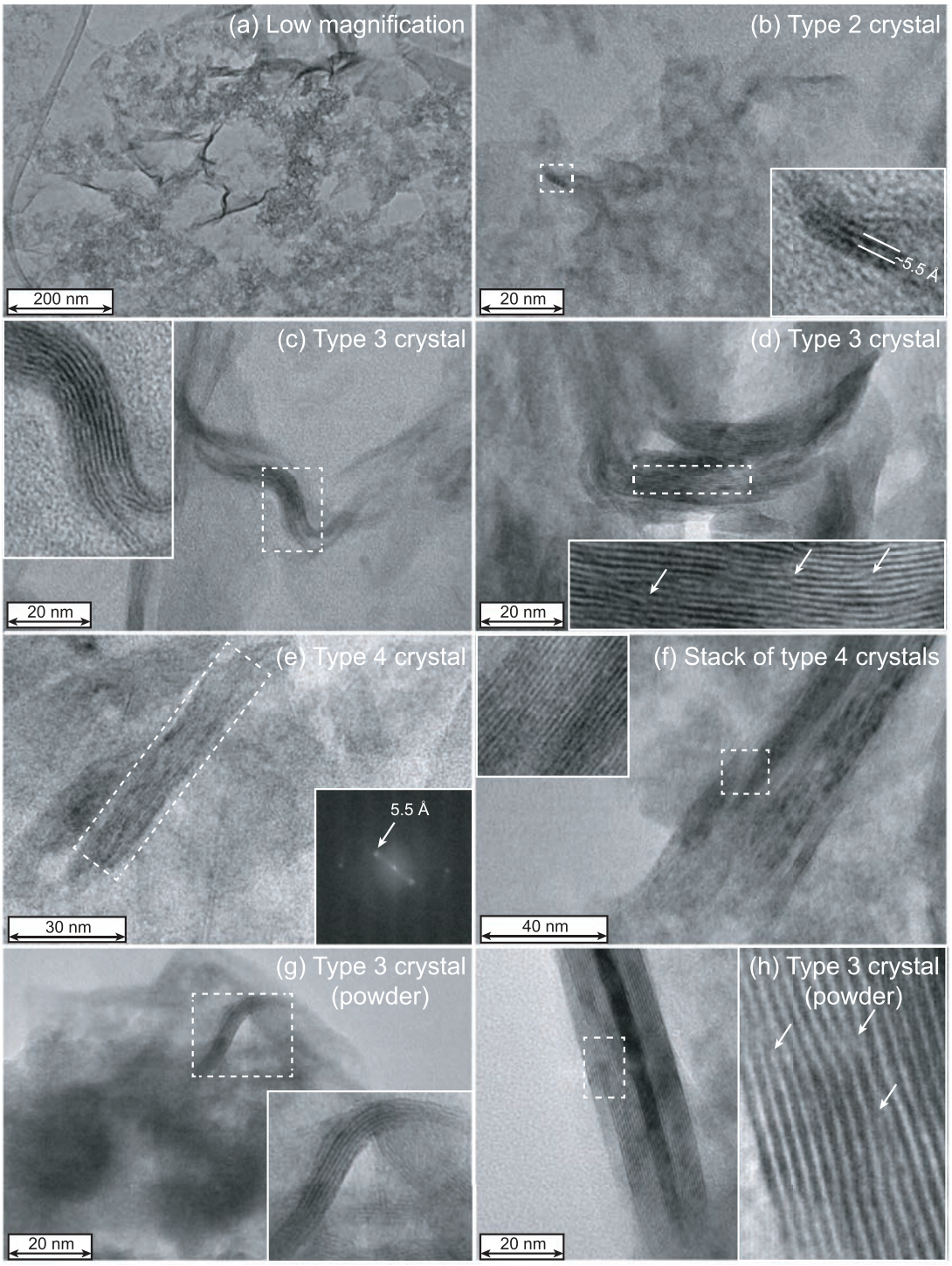

Fig. 4. TEM observation of MndBi-0.5. (a) Low-magnification view; (b) type-2 crystal; (c) and (d) type-3 crystals; (e) type-4 crystal; (f) crystal built from the stacking of type-4 crystals; (g) and (h) type-3 crystals deposited on the Cu grid from a drop of suspension instead of microtome preparation. Insets in (b), (c), (d), (f), (g) and (h) are enlarged views of regions delimited with dotted squares. In (d) and (h), arrows point to the presence of dislocations. The inset in (e) is a fast-Fourier transform (FFT) analysis of the region shown with a dotted square.

type-1 crystals. The crystal size in the layer plane was in good qualitative agreement with the XRD data, in which broad *hk* bands could be observed, indicative of crystallites ~5–10 nm in the layer plane (Lanson *et al.*, 2008; Grangeon *et al.*, 2012; Manceau *et al.*, 2013). On the other hand, the small crystal size perpendicular to the layer plane contrasted with the sharp 00*l* reflections. This apparent contradiction could be concealed assuming that TEM sample preparation procedure has delaminated δ-MnO_2 crystals.

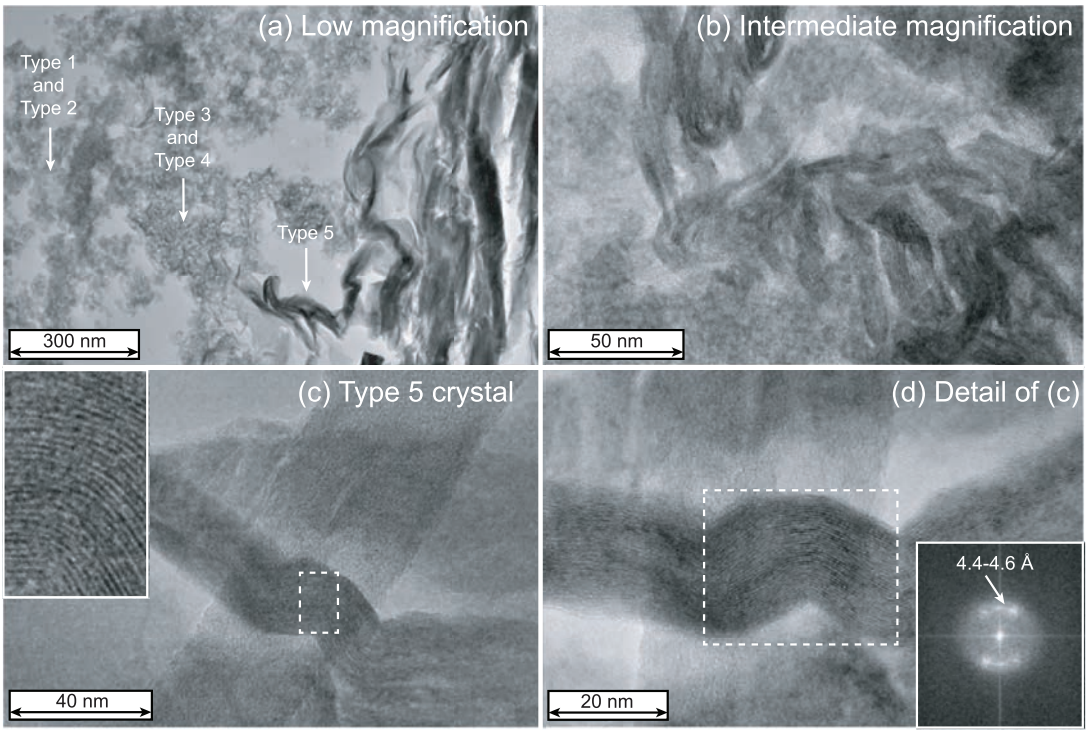

Fig. 5. TEM observation of MndBi-1.5. (a) Low-magnification view with the different crystal morphologies indicated with arrows; (b) type-5 crystals at intermediate magnification; (c) type-5 crystal exhibiting layer bending. The area shown with a dotted square in (c) is enlarged in the inset. (d) A detailed view of (c) and the inset is a FFT analysis of the region shown with a dotted square.

Observation of MndBi-0.5 evinced that a Mn^{2+} loading as low at 0.49 mmol g^{-1} led to the formation of crystals with contrasting morphologies and sizes, ranging ~10–200 nm in the layer plane (Fig. 4a). In addition to type-1 crystals, three types of such crystals were identified:

– Type-2 crystals had a size of ~10 nm in the layer plane, ~2–3 nm perpendicular, and were bent (Fig. 4b), probably as a result of the incorporation of $Mn^{3+}_{(s)}$ in layers containing mainly Mn^{4+}. The layer-to-layer distance was ~5.5 Å, typical for dehydrated phyllomanganates (Cygan *et al.*, 2012; Wegorzewski *et al.*, 2015). Dehydration was possibly induced by sample freeze-drying or by the secondary vacuum in the TEM. For type-1 and type-2 crystals having similar lateral dimensions, it is proposed that the latter formed from the coherent stacking of the former;
– Type-3 crystals were ~50 nm in the layer plane, and were built of ~10–20 layers stacked parallel to each other, with a layer-to-layer distance of ~5.5 Å (Fig. 4c, d). As type-2 crystals, they were bent. Images of the lateral terminations of type-3 crystals showed that they consisted of stacked type-2 crystals (Fig. 4c). Layer dislocations were observed also on some crystals (Fig. 4d), suggesting that type-2 crystals connected also within the layer plane to form type-3 crystals. Most likely, the type-3 crystals thus originated from the oriented aggregation of type-2 crystals, both within the layer plane and perpendicular to it;
– Type 4 crystals had lath-like shape, dimensions of ~50–100 nm in the layer plane and ~10–20 nm perpendicular (Fig. 4e), layer-to-layer distance of 5.5 Å (inset in Fig. 4e), and were rarely found as stacks (Fig. 4f). It is speculated that they resulted from the same aggregation mechanisms proposed for the type-3 crystals, but with fewer defects between connected type-2 crystals and/or a specific distribution of $Mn^{3+}_{(s)}$ so as to minimize layer strains and bending. Note that layer bending and dislocations observed in type-3 crystals cannot be related to sample preparation, as crystals deposited from a drop of a δ-MnO_2 suspension exhibited similar microstructural features (Fig. 4g, h).

These observations demonstrate that the surface of δ-MnO_2 is modified at loadings as low as 0.5 Mn^{2+} per nm^2. As a consequence, surface complexation models, which rely on a reversible sorption hypothesis (Tournassat *et al.*, 2013), may not be suited to describe Mn^{2+} interaction with δ-MnO_2.

All types of crystals found in samples with lower Mn^{2+} loadings were observed in MndBi-1.5 that contained also larger crystals (type-5), ~100–150 nm in the layer plane and ~20–30 nm perpendicular (Fig. 5a). In contrast, XRD indicated that MndBi-1.5 consisted mainly of isolated δ-MnO_2 nanosheets. However, type-5 crystals were bent (Fig. 5b). Bending did not involve layer disruption (Fig. 5c), but likely led to variable layer-to-layer distance, best quantified from FFT analysis of the images (Fig. 5d). This analysis showed that layer-to-layer distance varied within a given crystal, being equal to 4.4–4.6 Å. Both layer bending and layer-to-layer distance heterogeneity within a given crystal reduced crystallite size within the layer plane and led to vanishing of 00*l* reflection.

Finally, MndBi-28.1 contained, in addition to all previously mentioned types of crystals, type-6 crystals (Fig. 6) whose selected-area electron diffraction (SAED) patterns were typical for synthetic feitknechtite (Fig. 6c). These crystals were up to ~100 nm × 500 nm and were built of the stacking of laths resembling type-5 crystals but free of stacking defects and dislocations. These laths were not simply aligned, but were connected (Fig. 6d, e), as shown by both the observation of interference fringes (inset in Fig. 6e) and the FFT image analysis showing a homogeneous layer-to-layer distance (4.4 Å, inset in Fig. 6e). It is proposed that type-6 crystals formed from the oriented aggregation, perpendicular to the layer plane, of type-5 crystals. The presence of dislocations in type-5 crystals is thought to have inhibited their oriented aggregation. Bending was not observed either in type-6 crystals, possibly because all $Mn^{4+}_{(s)}$ was converted to $Mn^{3+}_{(s)}$, allowing for their specific distribution to accommodate their Jahn–Teller distortion. No Mn^{2+}-rich phase could be detected with SAED, despite a molar ratio of sorbed Mn^{2+} to structural δ-MnO_2 Mn of 3 (assuming a defect-free δ-MnO_2 and a molar mass of 119 g mol^{-1}, Giovanoli *et al.*, 1970). Consequently, it was concluded that part of the Mn^{2+} was sorbed by δ-MnO_2 and/or synthetic feitknechtite, or precipitated as an amorphous phase.

3.4. The role of oriented aggregation in nanoparticle growth

The present description of the vernadite-to-feitknechtite transformation, from macroscopic to crystal scales, is consistent with our current understanding of this transformation (Elzinga, 2011, 2016; Lefkowitz *et al.*, 2013; Lefkowitz & Elzinga, 2015). One of the key findings is the major role of oriented aggregation in the nucleation and growth of feitknechtite from δ-MnO_2 precursors. This process is increasingly recognized as one of the main processes responsible for nanoparticle growth (Penn, 2004; Niederberger & Colfen, 2006; Yuwono *et al.*, 2010): carbonates (Shen *et al.*, 2006), iron (Jia & Gao, 2008a and b) and manganese (Portehault *et al.*, 2007) oxides. It was also shown to be responsible for the phase transformations of nanoparticle precursors (*e.g.*, Hockridge *et al.*, 2009). Recently, oriented aggregation was shown to be involved in the formation of synthetic todorokite and cryptomelane from a δ-MnO_2 precursor (Chen *et al.*, 1986; Atkins *et al.*, 2014, 2016; Grangeon *et al.*, 2015) and in the change of δ-MnO_2 layer symmetry, from hexagonal to orthogonal (Zhao *et al.*, 2016). It is thus possible to speculate that Mn oxides found in surficial environments were to a large extent formed from vernadite precursors (Bodeï *et al.*, 2007; Xu *et al.*, 2010), possibly through oriented aggregation mechanisms.

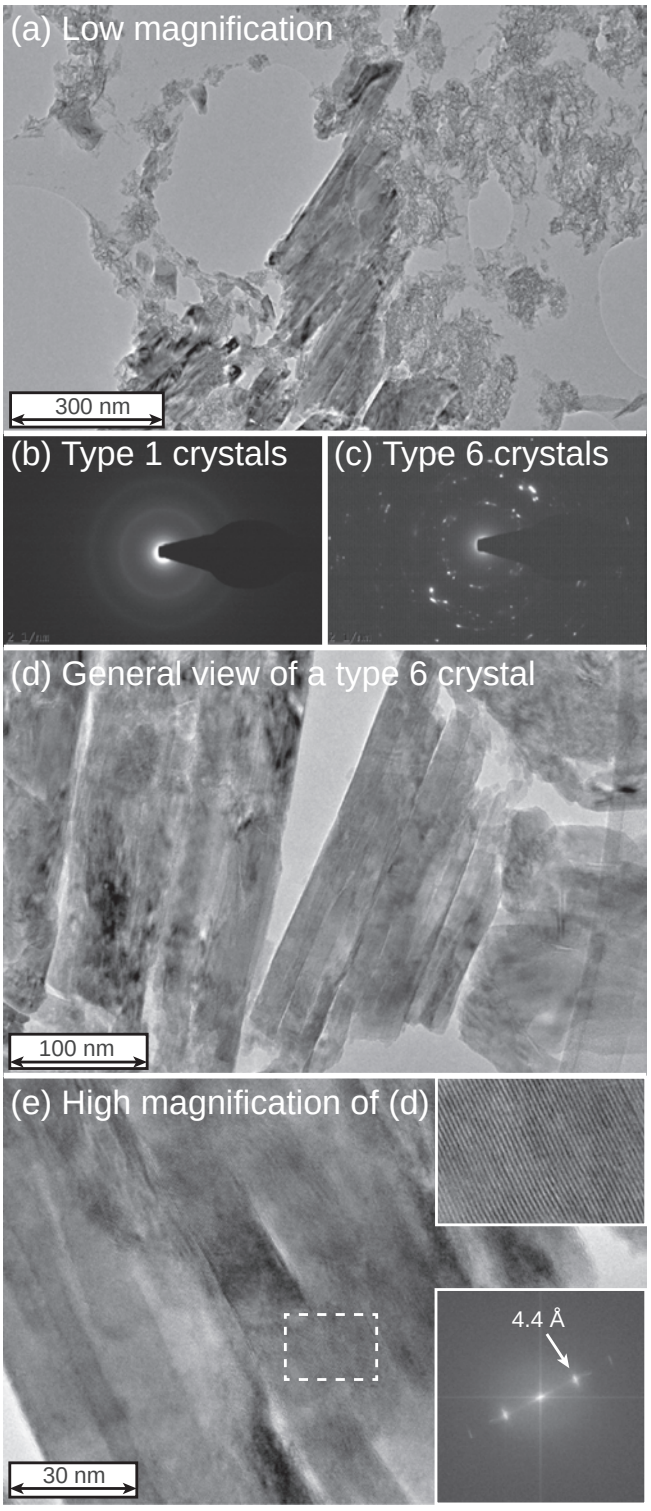

Fig. 6. TEM observation of MndBi-28.1. (a) Low-magnification view; (b) and (c) SAED patterns collected on the smallest crystals (top right in (a)) and the biggest crystals (centre in (a)), respectively; (d) and (e) type-6 crystal. The FFT analysis shown as an inset at the bottom right of (e) was calculated over the whole image while the inset at the top right is an enlarged view of the area delimited with a dotted square.

4. Concluding remarks: environmental implications

Vernadite with hexagonal layer symmetry is a sink for many trace elements in the environment. In natural settings were $Mn^{2+}_{(aq)}$ is abundant, such as in lake and marine water columns and in sediments (Burdige, 1993), interactions between vernadite and $Mn^{2+}_{(aq)}$ may induce morphological and mineralogical changes that could impact its reactivity and the fate of trace elements sorbed at its surface. Two main structural transformations were identified during reaction of δ-MnO_2 (synthetic vernadite) with $Mn^{2+}_{(aq)}$. At a low Mn^{2+} to δ-MnO_2 ratio (<3.27 mmol g^{-1}), δ-MnO_2 crystal size increased with $Mn^{2+}_{(aq)}$. At a Mn^{2+} to δ-MnO_2 ratio of 3.27 mmol g^{-1} or higher, δ-MnO_2 was converted to synthetic feitknechtite, and the size of synthetic feitknechtite crystals was observed to increase with $Mn^{2+}_{(aq)}$. δ-MnO_2 with orthogonal layer symmetry was not detected as a transformation intermediate, possibly because experiments were conducted at slightly acidic pH (Zhao *et al.*, 2016).

When crystal size increases, the specific surface area, and especially the contribution of particle edges to this surface, decreases. Vernadite edge sites being reactive (Simanova *et al.*, 2015), the increase in vernadite crystal size when in contact with $Mn^{2+}_{(aq)}$, even at low concentrations, can be detrimental to its trace-metal scavenging ability. By analogy, the same is expected for feitknechtite at high Mn^{2+} to δ-MnO_2 ratio. The impact of the vernadite-to-feitknechtite transformation on the fate of trace elements remains unclear, however. The lack of any significant dissolution of δ-MnO_2 potentially minimizes the release of trace metal elements along the reaction pathway, but their possible incorporation in the newly formed feitknechtite structure remains undocumented. Unlike tunnel structures, feitknechtite has been observed seldom in natural settings, probably because of its limited chemical stability and high sensitivity to fluctuation in redox conditions, which lead to its back-conversion to vernadite (Bargar *et al.*, 2005). Consequently, no data are currently available to evaluate the affinity of trace elements for feitknechtite in natural settings. Similar to tunnel structures (Liu *et al.*, 2004; Kumagai *et al.*, 2005; Cui *et al.*, 2011; Atkins *et al.*, 2014), additional insights into vernadite reactivity in suboxic systems and its impact on the fate of trace metals could probably be sought experimentally as feitknechtite is frequently observed in laboratory experiments mimicking natural conditions (Hem *et al.*, 1982; Murray *et al.*, 1985; Wang *et al.*, 2015).

Acknowledgements: S.G. acknowledges funding by the French National Research Agency (ANR, grant ANR-14-CE01-0006) and thanks Jacques Deparis, Nicolas Marty and Julie Philibert for fruitful discussions. SOLEIL data were acquired in the frame of proposal 20141260. A. Fernandez-Martinez and T. Conte are respectively thanked for help during XRD data collection and Mn^{2+} measurement. This article benefited from comments and suggestions by an anonymous reviewer and Alain Baronnet.

References

Appelo, C.A.J. & Postma, D. (1999): A consistent model for surface complexation on birnessite (δ-MnO_2) and its application to a column experiment. *Geochim. Cosmochim. Acta*, **63**, 3039–3048.

Atkins, A.L., Shaw, S., Peacock, C.L. (2014): Nucleation and growth of todorokite from birnessite: implications for trace-metal cycling in marine sediments. *Geochim. Cosmochim. Acta*, **144**, 109–125.

—, —, — (2016): Release of Ni from birnessite during transformation of birnessite to todorokite: implications for Ni cycling in marine sediments. *Geochim. Cosmochim. Acta*, **189**, 158–183.

Bargar, J.R., Tebo, B.M., Bergmann, U., Webb, S.M., Glatzel, P., Chiu, V.Q., Villalobos, M. (2005): Biotic and abiotic products of Mn(II) oxidation by spores of the marine *Bacillus* sp. strain SG-1. *Am. Mineral.*, **90**, 143–154.

Bargar, J.R., Fuller, C.C., Marcus, M.A., Brearley, A.J., Perez De la Rosa, M., Webb, S.M., Caldwell, W.A. (2009): Structural characterization of terrestrial microbial Mn oxides from Pinal Creek, AZ. *Geochim. Cosmochim. Acta*, **73**, 889–910.

Barrett, K.A. & McBride, M.B. (2005): Oxidative degradation of glyphosate and aminomethylphosphonate by manganese oxide. *Environ. Sci. Technol.*, **39**, 9223–9228.

Bellanca, A., Hauser, S., Neri, R., Palumbo, B. (1996): Mineralogy and geochemistry of Terra Rossa soils, western Sicily: insights into heavy metal fractionation and mobility. *Sci. Total Environ.*, **193**, 57–67.

Birnie, A.C. & Paterson, E. (1991): The mineralogy and morphology of iron and manganese oxides in an imperfectly-drained Scottish soil. *Geoderma*, **50**, 219–237.

Bodeï, S., Manceau, A., Geoffroy, N., Baronnet, A., Buatier, M. (2007): Formation of todorokite from vernadite in Ni-rich hemipelagic sediments. *Geochim. Cosmochim. Acta*, **71**, 5698–5716.

Boonfueng, T., Axe, L., Xu, Y., Tyson, T.A. (2006): The impact of Mn oxide coatings on Zn distribution. *J. Colloid Interface Sci.*, **298**, 615–623.

Bricker, O. (1965): Some stability relations in the system Mn–O_2–H_2O at 25° and one atmosphere total pressure. *Am. Mineral.*, **50**, 1296–1354.

Burdige, D.J. (1993): The biogeochemistry of manganese and iron reduction in marine sediments. *Earth-Sci. Rev.*, **35**, 249–284.

Chang Chien, S.W., Chen, H.L., Wang, M.C., Seshaiah, K. (2009): Oxidative degradation and associated mineralization of catechol, hydroquinone and resorcinol catalyzed by birnessite. *Chemosphere,* **74**, 1125–1133.

Chen, C.C., Golden, D.C., Dixon, J.B. (1986): Transformation of synthetic birnessite to cryptomelane – an electron-microscopic study. *Clays Clay Miner.*, **34**, 565–571.

Cheney, M.A., Sposito, G., McGrath, A.E., Criddle, R.S. (1996): Abiotic degradation of 2,4-D (dichlorophenoxyacetic acid) on synthetic birnessite: a calorespirometric method. *Colloid Surf. A*, **107**, 131–140.

Chukhrov, F.V., Sakharov, B.A., Gorshkov, A.I., Drits, V.A., Dikov, Y.P. (1985): Crystal structure of birnessite from the Pacific ocean. *Int. Geol. Rev.*, **27**, 1082–1088.

Cui, H.-J., Liu, F., Tan, W.-F., Feng, X.-H. (2011): Effect of cobalt-doped framework on formation of todorokite from layered manganese oxides with Mg^{2+}/Co^{2+} ions as template. *Pedosphere*, **21**, 730–737.

Cygan, R.T., Post, J.E., Heaney, P.J., Kubicki, J.D. (2012): Molecular models of birnessite and related hydrated layered minerals. *Am. Mineral.*, **97**, 1505–1514.

Drits, V.A., Lanson, B., Gaillot, A.-C. (2007): Birnessite polytype systematics and identification by powder X-ray diffraction. *Am. Mineral.*, **92**, 771–788.

Duff, M.C., Hunter, D.B., Triay, I.R., Bertsch, P.M., Reed, D.T., Sutton, S.R., Shea-McCarthy, G., Kitten, J., Eng, P., Chipera, S.J., Vaniman, D.T. (1999): Mineral associations and average oxidation states of sorbed Pu on tuff. *Environ. Sci. Technol.*, **33**, 2163–2169.

Elzinga, E.J. (2011): Reductive transformation of birnessite by aqueous Mn(II). *Environ. Sci. Technol.*, **45**, 6366–6372.

— (2016): ^{54}Mn radiotracers demonstrate continuous dissolution and reprecipitation of vernadite (δ-MnO_2) during interaction with aqueous Mn(II). *Environ. Sci. Technol.*, **50**, 8670–8677.

Elzinga, E.J. & Kustka, A.B. (2015): A Mn-54 radiotracer study of Mn isotope solid–liquid exchange during reductive transformation of vernadite (δ-MnO_2) by aqueous Mn(II). *Environ. Sci. Technol.*, **49**, 4310–4316.

Fendorf, S.E., Sparks, D.L., Franz, J.A., Camaioni, D.M. (1993): Electron paramagnetic resonance stopped-flow kinetic study of manganese(II) sorption–desorption on birnessite. *Soil Sci. Soc. Am. J.*, **57**, 57–62.

Fuller, C.C. & Bargar, J.R. (2014): Processes of zinc attenuation by biogenic manganese oxides forming in the hyporheic zone of Pinal Creek, Arizona. *Environ. Sci. Technol.*, **48**, 2165–2172.

Giovanoli, R. (1980): Vernadite is random-stacked birnessite. *Miner. Depos.*, **15**, 251–253.

Giovanoli, R., Stähli, E., Feitknecht, W. (1970): Über Oxidhydroxide des vierwertigen Mangans mit Schichtengitter. 1. Mitteilung: Natriummangan (II, III) manganat (IV). *Helv. Chim. Acta*, **59**, 209–220.

Grangeon, S., Lanson, B., Lanson, M., Manceau, A. (2008): Crystal structure of Ni-sorbed synthetic vernadite: a powder X-ray diffraction study. *Mineral. Mag.*, **72**, 1197–1209.

Grangeon, S., Lanson, B., Miyata, N., Tani, Y., Manceau, A. (2010): Structure of nanocrystalline phyllomanganates produced by freshwater fungi. *Am. Mineral.*, **95**, 1608–1616.

Grangeon, S., Manceau, A., Guilhermet, J., Gaillot, A.-C., Lanson, M., Lanson, B. (2012): Zn sorption modifies dynamically the layer and interlayer structure of vernadite. *Geochim. Cosmochim. Acta*, **85**, 302–313.

Grangeon, S., Lanson, B., Lanson, M. (2014): Solid-state transformation of nanocrystalline phyllomanganate into tectomanganate: influence of initial layer and interlayer structure. *Acta Crystallogr. B*, **70**, 828–838.

Grangeon, S., Fernandez-Martinez, A., Warmont, F., Gloter, A., Marty, N., Poulain, A., Lanson, B. (2015): Cryptomelane formation from nanocrystalline vernadite precursor: a high energy X-ray scattering and transmission electron microscopy perspective on reaction mechanisms. *Geochem. Trans.*, **16**, 12.

Grangeon, S., Fernandez-Martinez, A., Claret, F., Marty, N., Tournassat, C., Warmont, F., Gloter, A. (2017): In-situ determination of the kinetics and mechanisms of nickel adsorption by nanocrystalline vernadite. *Chem. Geol*., **459**, 24–31.

Halbach, P. (1986): Processes controlling the heavy metal distribution in Pacific ferromanganese nodules and crusts. *Int. J. Earth Sci.*, **75**, 235–247.

Hem, J.D., Roberson, C.E., Fournier, R.B. (1982): Stability of βMnOOH and manganese oxide deposition from springwater. *Water Resour. Res.*, **18**, 563–570.

Hochella Jr., M.F., Kasama, T., Putnis, A., Putnis, C.V., Moore, J.N. (2005): Environmentally important, poorly crystalline Fe/Mn hydrous oxides: ferrihydrite and a possibly new vernadite-like mineral from the Clark Fork River Superfund Complex. *Am. Mineral.*, **90**, 718–724.

Hockridge, J.G., Jones, F., Loan, M., Richmond, W.R. (2009): An electron microscopy study of the crystal growth of schwertmannite needles through oriented aggregation of goethite nanocrystals. *J. Cryst. Growth*, **311**, 3876–3882.

Jia, B. & Gao, L. (2008a): Growth of well-defined cubic hematite single crystals: oriented aggregation and ostwald ripening. *Cryst. Growth Des.*, **8**, 1372–1376.

—, — (2008b): Morphological transformation of Fe_3O_4 spherical aggregates from solid to hollow and their self-assembly under an external magnetic field. *J. Phys. Chem. C*, **112**, 666–671.

Johnson, K., Purvis, G., Lopez-Capel, E., Peacock, C., Gray, N., Wagner, T., März, C., Bowen, L., Ojeda, J., Finlay, N., Robertson, S., Worrall, F., Greenwell, C. (2015): Towards a mechanistic understanding of carbon stabilization in manganese oxides. *Nat. Commun.*, **6**, 7628.

Johnson, J.E., Savalia, P., Davis, R., Kocar, B.D., Webb, S.M., Nealson, K.H., Fischer, W.W. (2016): Real-time manganese phase dynamics during biological and abiotic manganese oxide reduction. *Environ. Sci. Technol.*, **50**, 4248–4258.

Jurgensen, A., Widmeyer, J.R., Gordon, R.A., Bendell-Young, L.I., Moore, M.M., Crozier, E.D. (2004): The structure of the manganese oxide on the sheath of the bacterium *Leptothrix discophora*: an XAFS study. *Am. Mineral.*, **89**, 1110–1118.

Koppi, A.J., Edis, R., Field, D.J., Geering, H.R., Klessa, D.A., Cockayne, D.J.H. (1996): Rare earth element trends and cerium–uranium–manganese associations in weathered rock from Koongarra, Northern Territory, Australia. *Geochim. Cosmochim. Acta*, **60**, 1695–1707.

Kumagai, N., Komaba, S., Abe, K., Yashiro, H. (2005): Synthesis of metal-doped todorokite-type MnO_2 and its cathode characteristics for rechargeable lithium batteries. *J. Power Sources*, **SI 146**, 310–314.

Kunzendorf, H. & Friedrich, G.H.W. (1976): The distribution of U and Th in growth zones of manganese nodules. *Geochim. Cosmochim. Acta*, **40**, 849–852.

Lanson, B., Drits, V.A., Silvester, E., Manceau, A. (2000): Structure of H-exchange hexagonal birnessite and its mechanism of formation from Na-rich monoclinic buserite at low pH. *Am. Mineral.*, **85**, 826–838.

Lanson, B., Marcus, M.A., Fakra, S., Panfili, F., Geoffroy, N., Manceau, A. (2008): Formation of Zn–Ca phyllomanganate nanoparticles in grass roots. *Geochim. Cosmochim. Acta*, **72**, 2478–2490.

Lefkowitz, J.P. & Elzinga, E.J. (2015): Impacts of aqueous Mn(II) on the sorption of Zn(II) by hexagonal birnessite. *Environ. Sci. Technol.*, **49**, 4886–4893.

Lefkowitz, J.P., Rouff, A.A., Elzinga, E.J. (2013): Influence of pH on the reductive transformation of birnessite by aqueous Mn(II). *Environ. Sci. Technol.*, **47**, 10364–10371.

Liu, J., Son, Y.C., Cai, J., Shen, X.F., Suib, S.L., Aindow, M. (2004): Size control, metal substitution, and catalytic application of cryptomelane nanomaterials prepared using cross-linking reagents. *Chem. Mater.*, **16**, 276–285.

Manceau, A., Drits, V.A., Silvester, E., Bartoli, C., Lanson, B. (1997): Structural mechanism of Co^{2+} oxidation by the phyllomanganate buserite. *Am. Mineral.*, **82**, 1150–1175.

Manceau, A., Marcus, M.A., Tamura, N., Proux, O., Geoffroy, N., Lanson, B. (2004): Natural speciation of Zn at the micrometer scale in a clayey soil using X-ray fluorescence, absorption, and diffraction. *Geochim. Cosmochim. Acta*, **68**, 2467–2483.

Manceau, A., Kersten, M., Marcus, M.A., Geoffroy, N., Granina, L. (2007): Ba and Ni speciation in a nodule of binary Mn oxide phase composition from Lake Baikal. *Geochim. Cosmochim. Acta*, **71**, 1967–1981.

Manceau, A., Marcus, M.A., Grangeon, S., Lanson, M., Lanson, B., Gaillot, A.C., Skanthakumar, S., Soderholm, L. (2013): Short-range and long-range order of phyllomanganate nanoparticles determined using high-energy X-ray scattering. *J. Appl. Crystallogr.*, **46**, 193–209.

Manceau, A., Lanson, M., Takahashi, Y. (2014): Mineralogy and crystal chemistry of Mn, Fe, Co, Ni, and Cu in a deep-sea Pacific polymetallic nodule. *Am. Mineral.*, **99**, 2068–2083.

Marcus, M.A., Manceau, A., Kersten, M. (2004): Mn, Fe, Zn and As speciation in a fast-growing ferromanganese marine nodule. *Geochim. Cosmochim. Acta*, **68**, 3125–3136.

Murray, J.W. (1975): The interaction of metal ions at the manganese dioxide–solution interface. *Geochim. Cosmochim. Acta*, **39**, 505–519.

Murray, J.W., Dillard, J.G., Giovanoli, R., Moers, H., Stumm, W. (1985): Oxidation of Mn(II): initial mineralogy, oxidation state and ageing. *Geochim. Cosmochim. Acta*, **49**, 463–470.

Nasser, A., Sposito, G., Cheney, M.A. (2000): Mechanochemical degradation of 2,4-adsorbed on synthetic birnessite. *Colloid Surf. A*, **163**, 117–123.

Niederberger, M. & Colfen, H. (2006): Oriented attachment and mesocrystals: non-classical crystallization mechanisms based on nanoparticle assembly. *Phys. Chem. Chem. Phys.*, **8**, 3271–3287.

Ounsy, M., Girardot, R., Saintin, K., Viguier, G. (2013): Online data reduction for high throughput beamlines. *in* "International Conference on Accelerators and Large Experimental Physics Control Systems, San Francisco, USA, 7–11 October 2013".

Peacock, C.L. & Sherman, D.M. (2007): Crystal-chemistry of Ni in marine ferromanganese crusts and nodules. *Am. Mineral.*, **92**, 1087–1092.

Peña, J., Kwon, K.D., Refson, K., Bargar, J.R., Sposito, G. (2010): Mechanisms of nickel sorption by a bacteriogenic birnessite. *Geochim. Cosmochim. Acta*, **74**, 3076–3089.

Penn, R.L. (2004): Kinetics of oriented aggregation. *J. Phys. Chem. B*, **108**, 12707–12712.

Portehault, D., Cassaignon, S., Baudrin, E., Jolivet, J.-P. (2007): Morphology control of cryptomelane type MnO_2 nanowires by soft chemistry. Growth mechanisms in aqueous medium. *Chem. Mater.*, **19**, 5410–5417.

Ross, S.J., Franzmeier, D.P., Roth, C.B. (1976): Mineralogy and chemistry of manganese oxides in some Indiana soils. *Soil Sci. Soc. Am. J.*, **40**, 137–143.

Schneider, C.A., Rasband, W.S., Eliceiri, K.W. (2012): NIH Image to ImageJ: 25 years of image analysis. *Nat. Methods*, **9**, 671–675.

Shen, Q., Wang, L., Huang, Y., Sun, J., Wang, H., Zhou, Y., Wang, D. (2006): Oriented aggregation and novel phase transformation of vaterite controlled by the synergistic effect of calcium dodecyl sulfate and n-pentanol. *J. Phys. Chem. B*, **110**, 23148–23153.

Simanova, A.A., Kwon, K.D., Bone, S.E., Bargar, J.R., Refson, K., Sposito, G., Peña, J. (2015): Probing the sorption reactivity of the edge surfaces in birnessite nanoparticles using nickel(II). *Geochim. Cosmochim. Acta*, **164**, 191–204.

Taylor, R.M. (1968): The association of manganese and cobalt in soils – further observations. *J. Soil Sci.*, **19**, 77–80.

Taylor, R., McKenzie, R., Norrish, K. (1964): The mineralogy and chemistry of manganese in some Australian soils. *Aust. J. Soil Res.*, **2**, 235–248.

Tonkin, J.W., Balistrieri, L.S., Murray, J.W. (2004): Modeling sorption of divalent metal cations on hydrous manganese oxide using the diffuse double layer model. *Appl. Geochem.*, **19**, 29–53.

Tournassat, C., Grangeon, S., Leroy, P., Giffaut, E. (2013): Modeling specific pH dependent sorption of divalent metals on montmorillonite surfaces. A review of pitfalls, recent achievements and current challenges. *Am. J. Sci.*, **313**, 395–451.

Tu, S.H., Racz, G.J., Goh, T.B. (1994): Transformations of synthetic birnessite as affected by pH and manganese concentration. *Clays Clay Miner.*, **42**, 321–330.

Villalobos, M., Toner, B., Bargar, J., Sposito, G. (2003): Characterization of the manganese oxide produced by *Pseudomonas putida* strain MnB1. *Geochim. Cosmochim. Acta*, **67**, 2649–2662.

Villalobos, M., Lanson, B., Manceau, A., Toner, B., Sposito, G. (2006): Structural model for the biogenic Mn oxide produced by *Pseudomonas putida*. *Am. Mineral.*, **91**, 489–502.

Wang, X., Lan, S., Zhu, M., Ginder-Vogel, M., Yin, H., Liu, F., Tan, W., Feng, X. (2015): The presence of ferrihydrite promotes abiotic formation of manganese (oxyhydr)oxides. *Soil Sci. Soc. Am. J.*, **79**, 1297–1305.

Webb, S.M., Tebo, B.M., Bargar, J.R. (2005): Structural characterization of biogenic Mn oxides produced in seawater by the marine *Bacillus* sp. strain SG-1. *Am. Mineral.*, **90**, 1342–1357.

Wegorzewski, A.V., Kuhn, T., Dohrmann, R., Wirth, R., Grangeon, S. (2015): Mineralogical characterization of individual growth structures of Mn-nodules with different Ni plus Cu content from the central Pacific Ocean. *Am. Mineral.*, **100**, 2497–2508.

Xin, X., Jiang, X., Su, J., Yan, X., Ni, J., Faeflen, S.J., Huang, X., Wright, A.L. (2016): Manganese oxide affects nitrification and ammonia oxidizers in subtropical and temperate acid forest soils. *Catena*, **137**, 24–30.

Xu, H., Chen, T., Konishi, H. (2010): HRTEM investigation of trilling todorokite and nano-phase Mn-oxides in manganese dendrites. *Am. Mineral.*, **95**, 556–562.

Yuwono, V.M., Burrows, N.D., Soltis, J.A., Penn, R.L. (2010): Oriented aggregation: formation and transformation of mesocrystal intermediates revealed. *J. Am. Chem. Soc.*, **132**, 2163–2165.

Zhao, H., Zhu, M., Li, W., Elzinga, E.J., Villalobos, M., Liu, F., Zhang, J., Feng, X., Sparks, D.L. (2016): Redox reactions between Mn(II) and hexagonal birnessite change its layer symmetry. *Environ. Sci. Technol.*, **50**, 1750–1758.

Zhu, M., Ginder-Vogel, M., Parikh, S.J., Feng, X.-H., Sparks, D.L. (2010): Cation effects on the layer structure of biogenic Mn-oxides. *Environ. Sci. Technol.*, **44**, 4465–4471.

Received 23 December 2016
Modified version received 20 March 2017
Accepted 21 May 2017